**Rapid Communications**

# High-$T_c$ superconductivity in CaKFe$_4$As$_4$ in absence of nematic fluctuations

W.-L. Zhang,[1,*] W. R. Meier,[2,3] T. Kong,[2,3] P. C. Canfield,[2,3] and G. Blumberg[1,4,†]

[1]*Department of Physics & Astronomy, Rutgers University, Piscataway, New Jersey 08854, USA*
[2]*Department of Physics and Astronomy, Iowa State University, Ames, Iowa 50011, USA*
[3]*Division of Materials Science and Engineering, Ames Laboratory, Ames, Iowa 50011, USA*
[4]*National Institute of Chemical Physics and Biophysics, Akadeemia tee 23, 12618 Tallinn, Estonia*

We employ polarization-resolved Raman spectroscopy to study the multiband stoichiometric $T_c = 35$ K superconductor CaKFe$_4$As$_4$. We do not detect Pomeranchuk-like electronic nematic fluctuations which were universally observed in the $XY$ ($B_{2g}$) symmetry Raman response for most families of the Fe-based superconductors. In the superconducting state we observe, consistent with a nodeless order parameter, a full spectral weight suppression at low energies and the emergence of a composite pair-breaking coherence feature at energies between 12 and 20 meV. We analyze the superconductivity-induced phonon self-energy effects and give an estimation for the electron-phonon coupling constant $\lambda^\Gamma = 0.0015$ which is insufficient to provide attraction for high-$T_c$ pairing.

*Introduction.* Understanding the pairing mechanism in Fe-based superconductors (FeSCs) remains in the focus of research not only due to a high superconducting transition temperature $T_c$, but also because of the interplay of superconductivity with other electronic degrees of freedom, nematicity and magnetism in particular [1–6].

Electronic nematicity has been universally observed for many families of FeSCs [7,8]. Furthermore, compositions that are in proximity to the nematic quantum critical point (QCP) often show the highest $T_c$ [7–11]. The $T_c$ enhancement near the QCP scenario was recently studied by several theoretical proposals [12–14].

Raman spectroscopy has been often used to study the superconducting (SC) order parameter [11,15–19], the dynamics of electronic nematic fluctuations [10,11,20,21], as well as electron-phonon ($e$-$p$) interactions [22–25]. The FeSCs are well suited to study the mechanisms of $T_c$ enhancement from an experimental point of view.

The recent discovery of a new class of stoichiometric and strictly tetragonal superconductors Ca$A$Fe$_4$As$_4$ ($A$ = K, Rb, Cs) with a rather high $T_c$ (31–36 K) provides an ideal platform for the spectroscopic investigation of FeSCs in a clean limit, and to decide if the nematicity is a necessary condition for high-$T_c$ superconductivity in FeSCs [26–30]. Although the pristine Ca$A$Fe$_4$As$_4$ compounds do not show a long-range magnetic order, an electron doping via substitution of Co or Ni for Fe suppresses $T_c$ and induces an exotic spin-vortex crystal order, while the system remains tetragonal even for the magnetically ordered phase [31–33].

*Crystallographic structure.* The CaKFe$_4$As$_4$ structure may be considered as a modification of the extensively studied tetragonal 122 family of FeSCs with the body-centered space group $I4/mmm$. For CaKFe$_4$As$_4$, every other plane of the Ca atoms is replaced by K, reducing the crystallographic
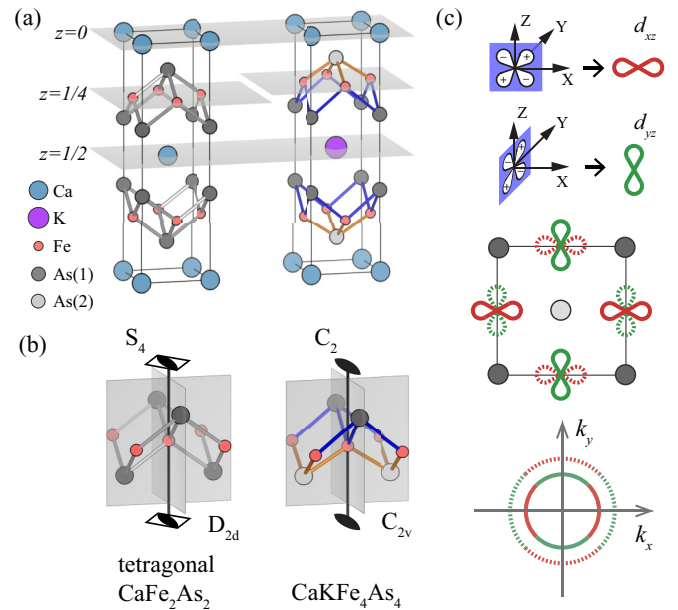


FIG. 1. (a) The comparison between CaFe$_2$As$_2$ and CaKFe$_4$As$_4$ lattice structures. For CaKFe$_4$As$_4$, the Fe sites are shifted away from the high-symmetry $z = 1/4$ and $3/4$ planes, causing two distinct As-Fe bond distances (shown in blue and orange). (b) The reduction of the Fe site symmetry from $D_{2d}$ for CaFe$_2$As$_2$ to $C_{2v}$ for CaKFe$_4$As$_4$. (c) For CaKFe$_4$As$_4$, a sketch of the partially occupied $d_{xz}/d_{yz}$ orbital order (the upper panel for real space), and derived two FS pockets in the vicinity of the $\Gamma$ point (the lower panel for momentum space). Solid and dotted lines denote differences in the orbital occupation which induce a static quadrupole moment on the Fe sites with a checkerboard order.

*weiluzhang41@gmail.com
†girsh@physics.rutgers.edu

space group to primitive $P4/mmm$ (point group $D_{4h}$) and therefore doubling the number of atoms in the primitive cell. In Figs. 1(a) and 1(b) we compare the tetragonal $CaFe_2As_2$ and $CaKFe_4As_4$ lattices.

For the body-centered $CaFe_2As_2$ structure the Fe layers are confined to the high-symmetry $z = 1/4$ and $3/4$ planes. All the Fe positions have $D_{2d}$ site symmetry with the $S_4$ axis along the $z$ direction, which imposes the degeneracy condition for Fe $3d_{xz}$ and $3d_{yz}$ orbitals. Such orbital degeneracy is a common feature for most of the FeSC structures [34,35].

It has been conjectured that degeneracy of the partially filled $d_{xz}/d_{yz}$ orbitals is a necessary condition for anomalously strong nematic effects in FeSCs: Such degeneracy enables dynamical charge oscillations in the sub-THz frequency range giving rise to a fluctuating charge ferroquadrupole moment with an amplitude proportional to the local oscillating charge imbalance $n_{xz} - n_{yz}$ [11]. The soft ferroquadrupole fluctuations often show critical behavior leading to a $d$-wave Pomeranchuk-like instability [11,36]. These fluctuations most dramatically manifest themselves in the low-frequency part of the $XY$-symmetry Raman response as an overdamped quasielastic feature in the normal state [10,11,20] which undergoes a metamorphosis into a coherent in-gap collective mode below $T_c$ [11,17–19,37,38].

In contrast to $Ba_{1-x}K_xFe_2As_2$ structure where $K^+$ substitute ions randomly occupy the host $Ba^{2+}$ sites, for $CaKFe_4As_4$ structure the $Ca^{2+}$ and $K^+$ ions are ordered in two distinct layers above and below the Fe-As layers. This layering of $Ca^{2+}/K^+$ ions causes the planes of Fe ions to shift vertically away from the high-symmetry positions [39,40]. The shift results in nonequivalent Fe-As bond distances for the As atoms above and below the Fe layer, thus the Fe site symmetry is reduced from $D_{2d}$ to $C_{2v}$ [Figs. 1(a) and 1(b)].

The removal of the $S_4$ symmetry on the Fe sites takes away the degeneracy of the partially occupied Fe $d_{xz}/d_{yz}$ orbitals [39], which gives rise to a static charge imbalance between these two orbitals, and hence creates a static $d_{x^2-y^2}$-symmetry quadrupole moment on each Fe site. Because the orbital character of the lower-energy state flips between the two neighboring Fe sites, the structure forms a static checkerboard antiquadrupole order [Fig. 1(c)]. The stiffness of the static antiquadrupole order parameter precludes Pomeranchuk-like fluctuations for the $CaKFe_4As_4$ compound.

In this Rapid Communication we study the charge dynamics in $CaKFe_4As_4$ single crystals by polarization-resolved Raman spectroscopy. We demonstrate that in contrast to the data from many FeSCs for which strong Pomeranchuk-like electronic nematic fluctuations give rise to an intense electronic Raman continuum in the $XY$-quadrupole symmetry channel, the electronic Raman signal for $CaKFe_4As_4$ is isotropic and generally weak. These data indeed support the notion that the quadrupole fluctuations for the $CaKFe_4As_4$ structure are quenched. Below $T_c$, we observe complete suppression of the low-frequency spectral intensity, indicating that all Fermi surface (FS) pockets are fully gapped, and transfer of the spectral weight to a composite SC coherence feature between 12 and 20 meV in the $XY$-symmetry electronic Raman response. We also observe a superconductivity-induced phonon self-energy effect and estimate the $e$-$p$ coupling to be weak, with a coupling constant $\lambda^{\Gamma} = 0.0015$.
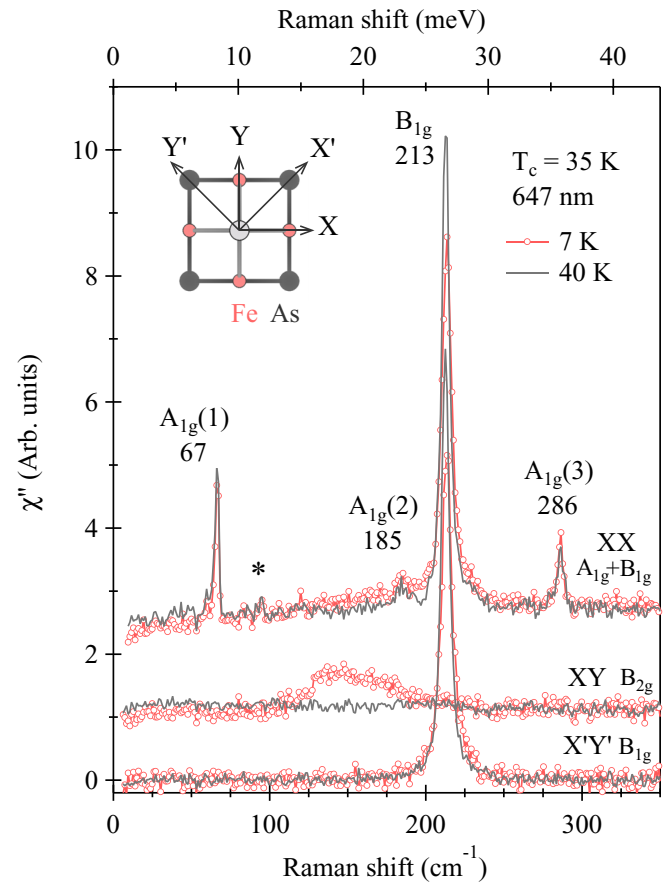


FIG. 2. Raman spectra for single-crystal $CaKFe_4As_4$ at 40 and 7 K. The $XY$ and $XX$ polarized spectra are offset by 1 and 2 units, respectively. Inset: Top view of the Fe-As layer and axis notations.

*Experiment.* Polarization-resolved Raman scattering measurements were performed in quasibackscattering geometry from the natural cleaved (001) surface. We use $\mu\nu = XX$, $XY$, and $X'Y'$ scattering geometries [41]. These geometries allow coupling to $A_{1g} + B_{1g}$, $B_{2g}$, and $B_{1g}$ symmetry excitations correspondingly.

The $CaKFe_4As_4$ single crystals ($T_c = 35$ K) used in this study were synthesized by the flux method [26,28]. The crystals were loaded into a continuous helium flow optical cryostat immediately after being cleaved in a nitrogen gas glove bag that is connected to the cryostat. For excitation we used the 647 nm line of a $Kr^+$ laser, where the laser beam was focused to a $50 \times 50$ $\mu$m spot. The laser power was kept below 10 mW in the normal state and 2.3 mW in the SC state. All referred temperatures are corrected for the laser heating. The Raman signal was collected and analyzed by a triple-grating spectrometer with 1.5 $cm^{-1}$ spectral resolution. Spectra were corrected for spectral response and background determined from the $X'Y'$-symmetry electronic continuum to obtain the Raman scattering intensity $I_{\mu\nu}(\omega, T)$ [42]. The Raman response function was derived as $\chi''_{\mu\nu}(\omega, T) = I_{\mu\nu}(\omega, T)/[1+n(\omega, T)]$, where $n(\omega, T)$ is the Bose distribution factor.

*Raman continuum and the superconducting gap.* In Fig. 2 we compare the Raman response above and below $T_c$ for three polarizations. Above $T_c$, besides four sharp phonon modes, the
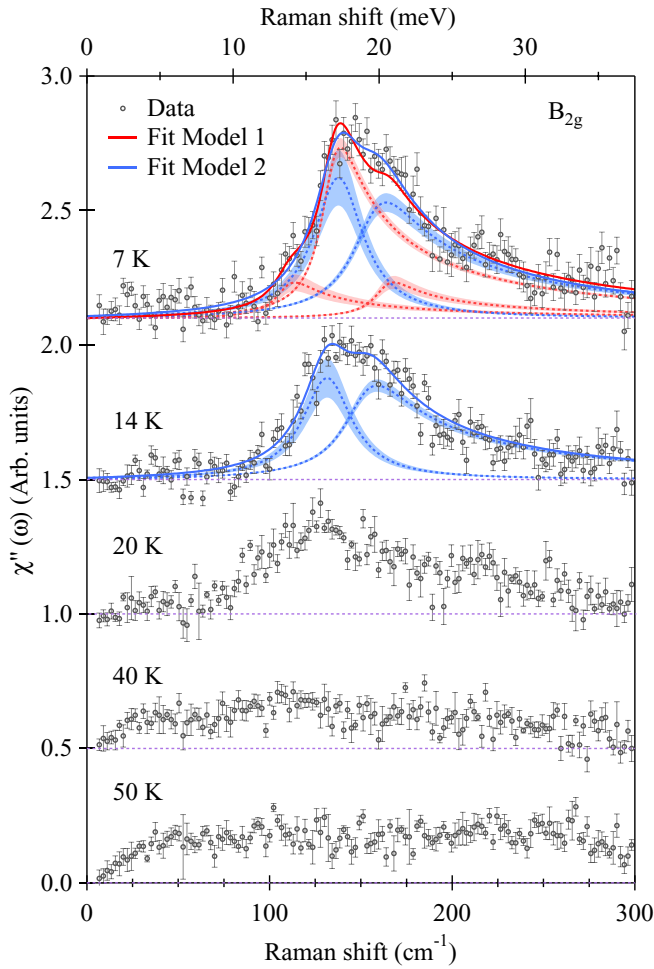
FIG. 3. Temperature evolution of the Raman response in the $B_{2g}$ channel. Error bars show one standard deviation. Red lines denote a model fit with three isotropic gap functions [15,43]. Another model fit comprising an isotropic gap and a shallow collective mode is shown in blue. The decompositions are shown by dotted lines, where shadings denote one standard deviation error.

spectra show a weak featureless electronic continuum for all polarizations. For the $XX$ and $X'Y'$ scattering geometries, the electronic continuum shows surprisingly little change across $T_c$, while for $XY$ polarization below $T_c$ the low-frequency spectral weight is transferred to a broad composite feature between 12 and 30 meV (100 and 240 cm$^{-1}$, see Fig. 3), which we relate to the formation of the SC gap on multiple FS pockets [15,44]. Upon cooling, the intensity of this feature grows, while the spectral intensity below 12 meV is completely suppressed at 7 K, implying that the SC gap is nodeless. We do not observe any sharp in-gap resonance modes below the composite gap feature.

For a multiband system the composite structure of the SC coherence feature could arise due to an overlap of several pair-breaking coherence peaks corresponding to gap values at different FS pockets [45]. An additional structure could also arise due to gap anisotropy on each FS pocket, or due to the appearance of a shallow in-gap collective mode [16,44,46,47]. The collective mode could be caused

TABLE I. Summary of fitting result at 7 K, units in meV.

| Model 1: Three SC gaps | Model 2: CM+SC gap |
|---|---|
| $2\Delta_1 = 13.6 \pm 0.6$ | $\omega_{CM} = 16.4 \pm 0.21$ |
| $2\Delta_2 = 16.8 \pm 0.1$ | $2\Delta_1 = 18.9 \pm 0.4$ |
| $2\Delta_3 = 20.2 \pm 0.2$ | |

by interactions both in particle-particle or in particle-hole channels [11,17,18,37,38,46,48].

In Fig. 3 we compare fits to the low-temperature data by two models: (i) The first model (shown in red), which conforms to the angle-resolved photoemission spectroscopy (ARPES) data [45], is composed of three pair-breaking coherence peaks arising due to isotropic gaps on three FS pockets $i$: $\chi'' = \sum_{i=1}^{3} \alpha_i \chi_i''$. Here, $\chi_i''(\omega, \Delta_i, T) = 4\Delta_i^2/\omega\sqrt{\omega^2 - 4\Delta_i^2} * L(\omega, T)$ denotes BCS coherence peaks with SC gap energies $2\Delta_i$ convoluted with $L(\omega, T)$ that accounts for temperature and instrumental broadening, and $\alpha_i$ denotes the weight of Raman coupling [15,43]. (ii) The second model (in blue) is composed of a collective mode (CM) due to electron-hole or particle-particle attraction in the $d_{xy}$-symmetry channel and a single pair-breaking coherence peak.

The energies resulting from the models are collected in Table I. Both models give satisfactory fits to the Raman data. However, the second model is hard to reconcile with one-electron spectroscopy data [45]. Furthermore, even if the second model containing a CM would apply, the interactions in the subdominant $d_{xy}$-wave channel cannot be strong because of the mode's small binding energy. This is in contrast to Ba$_{1-x}$K$_x$Fe$_2$As$_2$ at optimal doping [18,19], or to Na-111 [11] for which sharp in-gap CMs with significant binding energy have been reported.

*Phonon self-energy effects.* The CaKFe$_4$As$_4$ crystal (point group $D_{4h}$) contains ten atoms in a primitive cell. For the $\Gamma$ point phonons, group-theoretical symmetry decomposition yields $A_u + E_u$ acoustic modes, $4A_{2u} + 5E_u$ infrared active modes, $3A_{1g} + B_{1g} + 4E_g$ Raman active modes, and a $B_{2u}$ silent mode. For the experiments in backscattering geometry from the (001) surface, we observe all three $A_{1g}$ phonons and a $B_{1g}$ phonon (Fig. 2). The phonon energies and atomic displacements are summarized in Table II.

Above $T_c$ all modes exhibit a conventional temperature dependence: hardening and narrowing upon cooling due to anharmonic decay [49–51]. However, we note that the behavior for the $B_{1g}$ phonon mode in the SC state is anomalous: The mode's energy and linewidth increase upon cooling, as shown in Fig. 4(a). Similar phonon anomalies upon entering

TABLE II. Summary of Raman active phonons mode energies and atomic displacements for CaKFe$_4$As$_4$.

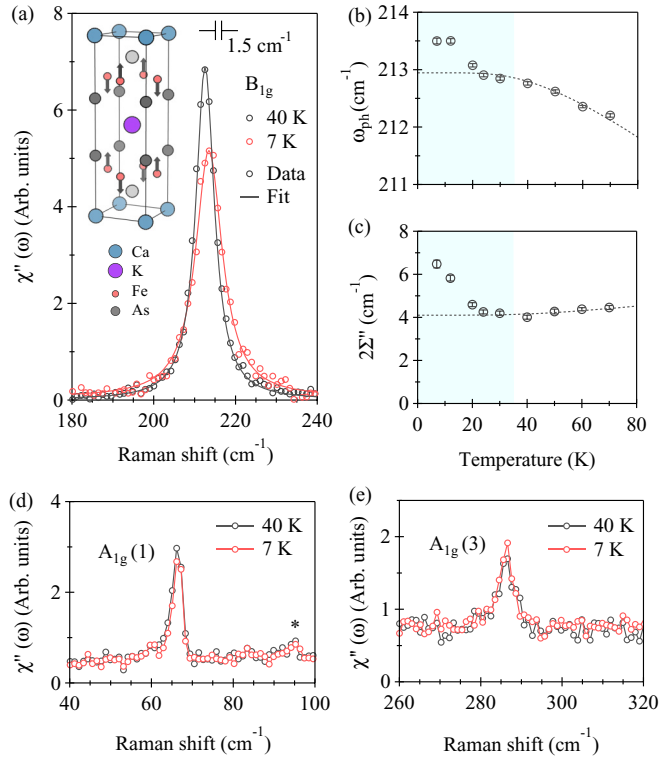| Symmetry | Energy at 40 K | Atomic displacements |
|---|---|---|
| $A_{1g}(1)$ | 67 cm$^{-1}$ | Fe$(z)$ + As(1)$(z)$ + As(2)$(z)$ |
| $A_{1g}(2)$ | 185 cm$^{-1}$ | Fe$(z)$ + As(1)$(z)$ + As(2)$(z)$ |
| $A_{1g}(3)$ | 286 cm$^{-1}$ | Fe$(z)$ + As(1)$(z)$ + As(2)$(z)$ |
| $B_{1g}(1)$ | 213 cm$^{-1}$ | Fe$(z)$ |

FIG. 4. Temperature evolution of phonon spectra. (a) The $B_{1g}$ phonon spectra and the fitting curve for above (40 K) and below (7 K) $T_c$. Inset of (a): Atomic displacements of the $B_{1g}$ phonon. (b), (c) Temperature dependence of $B_{1g}$ phonon energy $\omega_{ph}$ and linewidth $2\Sigma''$. $\Sigma''$ has been corrected for the spectrometer resolution as shown in (a). Dashed lines describe the anharmonic decay into two phonons obtained from the fit for the normal state. (d), (e) The $A_{1g}(1)$ and $A_{1g}(3)$ phonon modes at 40 and 7 K.

into a SC state were reported for MgB$_2$ [25] and for cuprate superconductors [22,23,52–55]. The behavior was explained by Zeyher-Zwicknagl's model [24] which implies that in the presence of electron-phonon coupling, the phonon self-energy is upward renormalized when the SC gap opens and the electronic density of states is pushed to the proximity of the phonon mode above the gap energies.

It is interesting to note that in contrast to the 67 cm$^{-1}$ $A_{1g}$ phonon (Fig. 2) that exhibits an asymmetric Fano line shape, the $B_{1g}$ phonon shows a nearly perfect Lorentzian shape. We attribute this to weak Raman coupling to the $B_{1g}$ symmetry electronic continuum: The $e$-$p$ interaction only renormalizes the phonon self-energy without showing a Fano interference in the spectra.

To quantify the superconductivity-induced self-energy effects and the $e$-$p$ interaction strength, we fit the phonon data with $\chi''_{ph}(\omega) \propto 4\omega_0 \Sigma'' [(\omega^2 - \omega_0^2 - 2\omega_0 \Sigma')^2 + 4(\omega_0 \Sigma'')^2]^{-1}$ function, where $\omega_0$ is the bare phonon frequency, and $\Sigma = \Sigma' + i\Sigma''$ is the complex phonon self-energy [24]. Thus, if $\Sigma$ is small, the mode appears at $\omega_{ph} = \sqrt{\omega_0^2 + 2\omega_0 \Sigma'}$ frequency. The fitting results are displayed in Figs. 4(b) and 4(c) [51].

We calculate the coupling constant $\lambda^\Gamma_{B_{1g}}$ around the $\Gamma$ point [56], $\lambda = -\kappa \sin u/u$, where $\kappa = \{[\Sigma'(7 \text{ K}) -$

$\Sigma'(40 \text{ K})] - i[\Sigma''(7 \text{ K}) - \Sigma''(40 \text{ K})]\}/\omega_{ph}(40 \text{ K})$ and $u \equiv \pi + 2i \cosh^{-1}[\omega_{ph}(40 \text{ K})/2\Delta]$. Using the energy of the strongest pair-breaking peak $2\Delta = 135$ cm$^{-1}$, we acquire a weak $e$-$p$ coupling constant $\lambda^\Gamma_{B_{1g}} \approx 0.0015$. The $A_{1g}$ phonons do not show measurable renormalization [Figs. 4(d) and 4(e)]. Therefore, the $B_{1g}$ mode is the only phonon that exhibits the SC-induced self-energy effects. Thus, we use $\lambda^\Gamma_{B_{1g}}$ to approximate the total $e$-$p$ coupling constant $\lambda$ [57].

In comparison, for a conventional phonon-mediated superconductor MgB$_2$ with a similar $T_c = 39$ K, a much larger coupling constant $\lambda = 0.2$ was derived from SC-induced phonon renormalization [25]. Thus, for CaKFe$_4$As$_4$, the value $\lambda$ is far from being sufficient to result in superconductivity with $T_c$ at 35 K.

*Conclusions.* In summary, we report a polarization-resolved Raman spectroscopic study of the single-crystal CaKFe$_4$As$_4$ superconductor with $T_c$ at 35 K.

Above $T_c$ we do not detect Pomeranchuk-like electronic nematic (quadrupole) fluctuations, which implies that the electronic nematicity may not be essential for high-$T_c$ superconductivity in FeSCs. Below $T_c$ we observe the development of a composite coherence feature between 12 and 20 meV in the $B_{2g}$ symmetry channel and a complete suppression of low-frequency spectral weight, which implies that all the FS pockets remain nodeless. We do not detect any sharp in-gap collective modes which were commonly observed for FeSCs which exhibit strong electronic nematic fluctuations.

We also study the SC-induced self-energy effects for Raman-active phonons and provide an estimate of the electron-phonon coupling constant $\lambda^\Gamma = 0.0015$, which is very small for a superconductor with $T_c$ at 35 K.

Because both the electronic nematic fluctuations and the superconductivity-induced self-energy effects for even-symmetry phononic modes are neglectfully small, we conclude that the spin fluctuations are primarily responsible for the pairing interaction in CaKFe$_4$As$_4$. In this case, the expected pairing symmetry is $s_\pm$, which is consistent with the observation of the spin-resonance mode at nesting vector $(\pi, \pi)$ by inelastic neutron scattering [58].

*Note added.* Recently, we became aware of a related Raman study [47]. The authors of Ref. [47] interpret features at 134 cm$^{-1}$ (16.6 meV) and at 50 cm$^{-1}$ (6.2 meV) as Bardasis-Schrieffer (BS) collective modes and argue that the appearance of the modes implies subdominant $d$-wave pairing interactions. We note here that none of the referred features in Raman spectra have a structure of a defined long-lived resonance. As such, assignments to any collective mode are difficult to support. Furthermore, the statement that there exist two independent attractive subdominant $XY$-symmetry pairing channels is unjustified.

[1] J. Paglione and R. L. Greene, Nat. Phys. **6**, 645 (2010).

[2] F. Wang and D.-H. Lee, Science **332**, 200 (2011).

[3] A. Chubukov, Annu. Rev. Condens. Matter Phys. **3**, 57 (2012).

[4] R. M. Fernandes, A. V. Chubukov, and J. Schmalian, Nat. Phys. **10**, 97 (2014).

[5] P. J. Hirschfeld, C. R. Phys. **17**, 197 (2016).

[6] Q. Si, R. Yu, and E. Abrahams, Nat. Rev. Mater. **1**, 16017 (2016).

[7] J.-H. Chu, H.-H. Kuo, J. G. Analytis, and I. R. Fisher, Science **337**, 710 (2012).

[8] H.-H. Kuo, J.-H. Chu, J. C. Palmstrom, S. A. Kivelson, and I. R. Fisher, Science **352**, 958 (2016).

[9] T. Shibauchi, A. Carrington, and Y. Matsuda, Annu. Rev. Condens. Matter Phys. **5**, 113 (2014).

[10] Y. Gallais, R. M. Fernandes, I. Paul, L. Chauvière, Y.-X. Yang, M.-A. Méasson, M. Cazayous, A. Sacuto, D. Colson, and A. Forget, Phys. Rev. Lett. **111**, 267001 (2013).

[11] V. K. Thorsmølle, M. Khodas, Z. P. Yin, C. Zhang, S. V. Carr, P. Dai, and G. Blumberg, Phys. Rev. B **93**, 054515 (2016).

[12] S. Lederer, Y. Schattner, E. Berg, and S. A. Kivelson, Phys. Rev. Lett. **114**, 097001 (2015).

[13] M. A. Metlitski, D. F. Mross, S. Sachdev, and T. Senthil, Phys. Rev. B **91**, 115111 (2015).

[14] D. Labat and I. Paul, Phys. Rev. B **96**, 195146 (2017).

[15] M. V. Klein and S. B. Dierker, Phys. Rev. B **29**, 4976 (1984).

[16] T. P. Devereaux and R. Hackl, Rev. Mod. Phys. **79**, 175 (2007), and references therein.

[17] Y. Gallais, I. Paul, L. Chauvière, and J. Schmalian, Phys. Rev. Lett. **116**, 017001 (2016).

[18] S.-F. Wu, P. Richard, H. Ding, H.-H. Wen, G. Tan, M. Wang, C. Zhang, P. Dai, and G. Blumberg, Phys. Rev. B **95**, 085125 (2017).

[19] T. Böhm, F. Kretzschmar, A. Baum, M. Rehm, D. Jost, R. H. Ahangharnejhad, R. Thomale, C. Platt, T. A. Maier, W. Hanke, B. Moritz, T. P. Devereaux, D. J. Scalapino, S. Maiti, P. J. Hirschfeld, P. Adelmann, T. Wolf, H.-H. Wen, and R. Hackl, arXiv:1703.07749.

[20] F. Kretzschmar, T. Bohm, U. Karahasanovic, B. Muschler, A. Baum, D. Jost, J. Schmalian, S. Caprara, M. Grilli, C. Di Castro, J. G. Analytis, J. H. Chu, I. R. Fisher, and R. Hackl, Nat. Phys. **12**, 560 (2016).

[21] S.-F. Wu, W.-L. Zhang, L. Li, H. B. Cao, H.-H. Kung, A. S. Sefat, H. Ding, P. Richard, and G. Blumberg, arXiv:1712.06066.

[22] S. L. Cooper, M. V. Klein, B. G. Pazol, J. P. Rice, and D. M. Ginsberg, Phys. Rev. B **37**, 5920(R) (1988).

[23] C. Thomsen, M. Cardona, B. Gegenheimer, R. Liu, and A. Simon, Phys. Rev. B **37**, 9860(R) (1988).

[24] R. Zeyher and G. Zwicknagl, Z. Phys. B **78**, 175 (1990).

[25] A. Mialitsin, B. S. Dennis, N. D. Zhigadlo, J. Karpinski, and G. Blumberg, Phys. Rev. B **75**, 020509(R) (2007).

[26] W. R. Meier, T. Kong, U. S. Kaluarachchi, V. Taufour, N. H. Jo, G. Drachuck, A. E. Böhmer, S. M. Saunders, A. Sapkota, A. Kreyssig, M. A. Tanatar, R. Prozorov, A. I. Goldman, F. F. Balakirev, A. Gurevich, S. L. Bud'ko, and P. C. Canfield, Phys. Rev. B **94**, 064501 (2016).

[27] A. Iyo, K. Kawashima, T. Kinjo, T. Nishio, S. Ishida, H. Fujihisa, Y. Gotoh, K. Kihou, H. Eisaki, and Y. Yoshida, J. Am. Chem. Soc. **138**, 3410 (2016).

[28] W. R. Meier, T. Kong, S. L. Bud'ko, and P. C. Canfield, Phys. Rev. Mater. **1**, 013401 (2017).

[29] R. Yang, Y. Dai, B. Xu, W. Zhang, Z. Qiu, Q. Sui, C. C. Homes, and X. Qiu, Phys. Rev. B **95**, 064506 (2017).

[30] K. Kawashima, S. Ishida, H. Fujihisa, Y. Gotoh, K. Kihou, Y. Yoshida, H. Eisaki, H. Ogino, and A. Iyo, J. Phys. Chem. Lett. **9**, 868 (2018).

[31] W. R. Meier, Q.-P. Ding, A. Kreyssig, S. L. Bud'ko, A. Sapkota, K. Kothapalli, V. Borisov, R. Valentí, C. D. Batista, P. P. Orth, R. M. Fernandes, A. I. Goldman, Y. Furukawa, A. E. Böhmer, and P. C. Canfield, npj Quantum Mater. **3**, 5 (2018).

[32] U. S. Kaluarachchi, V. Taufour, A. Sapkota, V. Borisov, T. Kong, W. R. Meier, K. Kothapalli, B. G. Ueland, A. Kreyssig, R. Valentí, R. J. McQueeney, A. I. Goldman, S. L. Bud'ko, and P. C. Canfield, Phys. Rev. B **96**, 140501(R) (2017).

[33] L. Xiang, W. R. Meier, M. Xu, U. S. Kaluarachchi, S. L. Bud'ko, and P. C. Canfield, Phys. Rev. B **97**, 174517 (2018).

[34] V. Cvetkovic and O. Vafek, Phys. Rev. B **88**, 134510 (2013).

[35] J. Hu and N. Hao, Phys Rev X **2**, 021009 (2012).

[36] Y. A. Pomeranchuk, Sov. Phys. JETP **8**, 361 (1958).

[37] M. Khodas, A. V. Chubukov, and G. Blumberg, Phys. Rev. B **89**, 245134 (2014).

[38] S. Maiti, A. V. Chubukov, and P. J. Hirschfeld, Phys. Rev. B **96**, 014503 (2017).

[39] F. Lochner, F. Ahn, T. Hickel, and I. Eremin, Phys. Rev. B **96**, 094521 (2017).

[40] J. Cui, Q.-P. Ding, W. R. Meier, A. E. Böhmer, T. Kong, V. Borisov, Y. Lee, S. L. Bud'ko, R. Valentí, P. C. Canfield, and Y. Furukawa, Phys. Rev. B **96**, 104512 (2017).

[41] $\mu\nu$ is short for $\bar{Z}(\mu\nu)Z$ in Porto's notation.

[42] The background is determined from the $X'Y'$ symmetry scattering intensity after subtracting the $B_{1g}$ phonon (see Supplement I in Ref. [59]).

[43] G. Blumberg, A. Mialitsin, B. Dennis, N. Zhigadlo, and J. Karpinski, Physica C **456**, 75 (2007).

[44] C. Sauer and G. Blumberg, Phys. Rev. B **82**, 014525 (2010).

[45] D. Mou, T. Kong, W. R. Meier, F. Lochner, L.-L. Wang, Q. Lin, Y. Wu, S. L. Bud'ko, I. Eremin, D. D. Johnson, P. C. Canfield, and A. Kaminski, Phys. Rev. Lett. **117**, 277001 (2016).

[46] M. V. Klein, Phys. Rev. B **82**, 014507 (2010).

[47] D. Jost, J.-R. Scholz, U. Zweck, W. R. Meier, A. E. Böhmer, P. C. Canfield, N. Lazarević, and R. Hackl, Phys. Rev. B **98**, 020504(R) (2018).

[48] A. V. Chubukov, I. Eremin, and M. M. Korshunov, Phys. Rev. B **79**, 220501 (2009).

[49] P. G. Klemens, Phys. Rev. **148**, 845 (1966).

[50] J. Menéndez and M. Cardona, Phys. Rev. B **29**, 2051 (1984).

[51] $\omega_{ph}(T) = \omega_{ph}(0) - \omega_1(1 + 2/\{\exp[\omega_{ph}(0)/k_BT]-1\})$, $\Sigma''(T) = \Sigma''(0) + \Gamma_1(1 + 2/\{\exp[\omega_{ph}(0)/k_BT] - 1\})$ are used to fit $\omega_{ph}(T)$ and $\Sigma''(T)$ for the normal state [49]. The dashed curves in Figs. 4(b) and 4(c) are plotted with the fitting result $\omega_{ph}(0) = 216.0 \pm 0.1$ cm$^{-1}$, $\omega_1 = 3.1 \pm 0.1$ cm$^{-1}$, $\Sigma''(0) = 2.2 \pm 0.3$ cm$^{-1}$, and $\Gamma_1 = 0.6 \pm 0.3$ cm$^{-1}$.

[52] B. Friedl, C. Thomsen, and M. Cardona, Phys. Rev. Lett. **65**, 915 (1990).

[53] K. F. McCarty, H. B. Radousky, J. Z. Liu, and R. N. Shelton, Phys. Rev. B **43**, 13751(R) (1991).

[54] G. Blumberg, M. V. Klein, L. Börjesson, R. Liang, and W. N. Hardy, J. Supercond. **7**, 445 (1994).

[55] C. Thomsen and M. Cardona, Raman scattering in high-$T_c$ superconductors, in *Physical Properties of High Temperature Superconductors I*, edited by D. M. Ginsberg (World Scientific, Singapore, 1998), Chap. 8, pp. 409–507.

[56] C. O. Rodriguez, A. I. Liechtenstein, I. I. Mazin, O. Jepsen, O. K. Andersen, and M. Methfessel, Phys. Rev. B **42**, 2692(R) (1990).

[57] Because the electron-phonon coupling strength is not expected to change markedly with phonon dispersion, $\lambda_{B1g}^{\Gamma}$ can be used to approximate the total $e$-$p$ coupling.

[58] K. Iida, M. Ishikado, Y. Nagai, H. Yoshida, A. D. Christianson, N. Murai, K. Kawashima, Y. Yoshida, H. Eisaki, and A. Iyo, J. Phys. Soc. Jpn. **86**, 093703 (2017).

[59] W.-L. Zhang, S.-F. Wu, S. Kasahara, T. Shibauchi, Y. Matsuda, and G. Blumberg, arXiv:1710.09892.